

Ground Penetrating Radar Based Subsurface Imaging of Targeted Buried Objects

T. Kishan Rao¹, E. G. Rajan

¹Research Scholar, MG-NIRSA, University of Mysore, India Former Executive Engineer, Irrigation Department Government of Telangana, India

²Adjunct Professor, Department of Cybernetics University of Petroleum and Energy Studies, Dehradun, India Hon. Director MG-NIRSA, Hyderabad, India

ABSTRACT

This paper provides a theoretical description as how a targeted buried object is detected using a ground penetrating radar. GPR systems work in two different modes (i) monostatic mode, and (ii) bistatic mode. In the monostatic mode, the transmitter antenna and receiver antenna of a GPR are collocated. In the case of bistatic mode, the transmitter antenna and the receiver antenna are kept separately but with a fixed distance between them. By moving, for instance, a monostatic GPR antenna system along a preselected line over the ground surface, which is called B-scan, one can obtain a two-dimensional reflection profile called radargram. At every position of the GPR antenna on the ground, an echo is obtained. Signals emitted by a GPR antenna spread in the form of a fan while scanning. The radiated signal ray broadens when it passes through the ground's subsurface. Due to this, a buried object would be visible in the radar console before and after moving over the object. That is why a point-shaped buried object will show up as an inverted hyperbola on the received image data. Mathematical description of various kinds of GPR related activities are briefly presented in this paper.

Keywords: Ground Penetrating Radar, Subsurface Imaging, Targeted Buried Object Detection

Date of Submission: 08-12-2020

Date of Acceptance: 24-12-2020

I. INTRODUCTION

While radar systems work in a free-space environment, GPRs work in media that exhibit electromagnetic properties, which are frequency-dependent. So, the reflected electromagnetic energy shows dispersive effects. Radar systems are used to detect targets at ranges of hundreds of kilometers, but in the case of GPR, targets at ranges of some meters only are detected because of limitation in the transmitted power and attenuation of the reflected signal. Moreover, resolution of GPR is very much limited to centimetres or metres (based on the active frequencies, which are smaller when compared to

those used in tactical radar systems). In any case, one has to employ frequencies ranging from tens of MHz to some GHz in order to achieve good spatial resolution of the reflected data. Different GPR configurations are used in land surveys and their choice is made based on different applications like (i) the type of exploration to be made, (ii) the type of targets to be detected, and (iii) the extent of region to be explored. For example, the region to be explored is studied initially by an aerial survey. Fig. 1 shows the image of an area obtained using a drone camera.



Fig. 1: Image of an area to be prospected

GPR Configurations for Data Collection and Measurement

GPR systems work in two different modes (i) monostatic mode, and (ii) bistatic mode. In the monostatic mode, the transmitter antenna and receiver antenna of a GPR are collocated. Fig. 2 shows a monostatic mode GPR architecture. In the case of bistatic mode, the transmitter antenna and the receiver antenna are kept separately but with a fixed distance between them. While moving the GPR along a predetermined survey line (profile), the

distance between these antennas is kept unchanged. Let us consider the monostatic mode GPR to be used for prospecting a land of interest. By moving, for instance, a monostatic GPR antenna system along a preselected line over the ground surface, which is called B-scan, one can obtain a two-dimensional reflection profile called radargram. At every position of the GPR antenna on the ground, an echo is obtained. Signals emitted by a GPR antenna spread in the form of a fan while scanning.

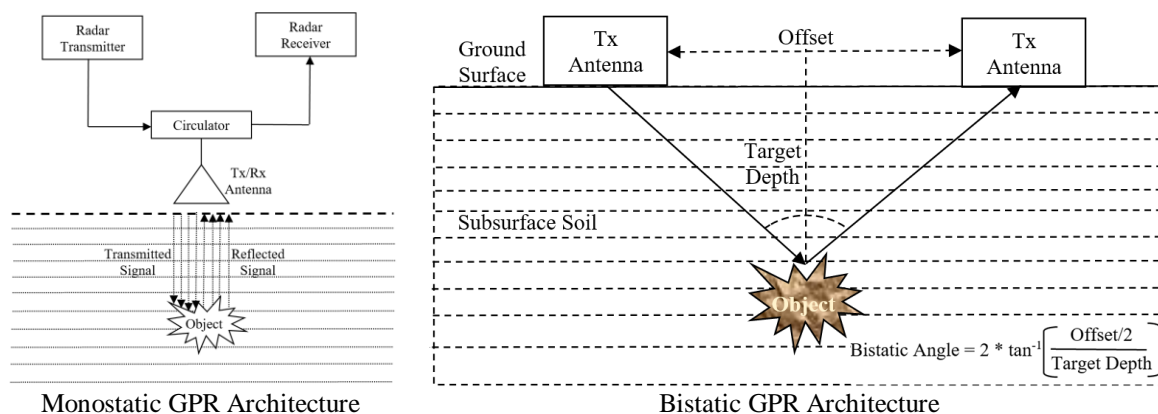


Fig. 2: Monostatic and Bistatic GPR Architectures

The radiated signal ray broadens when it passes through the ground's subsurface. Due to this, a buried object would be visible in the radar console before and after moving over the object. That is why

a point-shaped buried object will show up as an inverted hyperbola on the received image data. Fig. 3 shows this phenomenon.

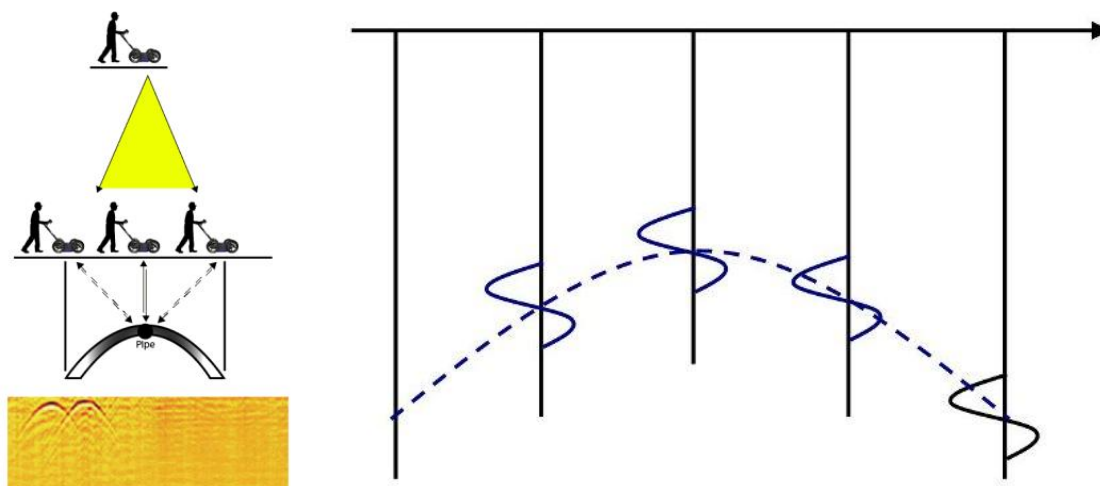


Fig. 3: Radargram slice of a scanned object and a hypothetical description of the radar response of a point-object

When the GPR antenna is kept directly over a target, the signal echo will be at the highest point of the inverted hyperbola on the data. Such a 2D radargram provides an approximate information about the presence and location of the target. But the actual shape of the target would be blurred due to

propagation and scattering of the electromagnetic wave in the soil. Let us consider a point-object, which is size wise small in terms of wavelength of the transmitted electromagnetic power. The reflected echo signals on moving the transmitter antenna along the predetermined profile yield a 2D

radargram image containing an inverted hyperbola corresponding to the point object. Let the position of the TX/RX system along the measurement line be x and $(0, d)$ be the position of the point-object. Then, the two-way travel-time is calculated using the equation

$$t = 2\sqrt{x^2 + d^2}/v$$

where v is the velocity of the electromagnetic wave in the soil. Now, the recorded image data shows an inverted hyperbola with a vertical axis and the apex at $(0, 2d/v)$. The shape of the inverted hyperbola depends on (i) the electromagnetic properties of the medium that decides the velocity, (ii) the GPR configuration, which is either monostatic or bistatic, and (iii) the depth of the point object which is the scatterer.

2. GPR subsurface imaging

The aim of GPR based subsurface imaging is to obtain radargram images for subsurface truth evaluation, that is, to obtain a visual knowledge representation of the scene below the ground surface. There are many requirements of subsurface imaging using a GPR. The basic requirement is to detect a buried object by its scattered signals. Next

requirement is to evaluate the physical size of the buried object. Yet another requirement is to study the subsurface scene with the help of various scatterers. In any case, subsurface imaging is a case of inverse scattering of microwave frequencies wherein the scatterers are reconstructed as a spatial map of the dielectric nature of various elements below the ground. This amounts to saying that subsurface imaging is a nonlinear problem for which one has to devise a procedure that is optimistic for a particular requirement. Many nonlinear imaging schemes have been developed till date; yet all such techniques pose the common problem of 'reliability'. Moreover, subsurface imaging deals with image data of very large size and thus a very large database has to be processed within given amount of time. This calls for development of fast and robust imaging algorithms with a high degree of reliability. Fig. 4 shows a 2D radargram of size 256×256 obtained using a GPR. This radargram is also called Vertical Seismic Profile (VSP). Fig. 4 shows a radargram obtained by B-scan, that is, moving a GPR antenna from a given position to another along a predetermined profile line.

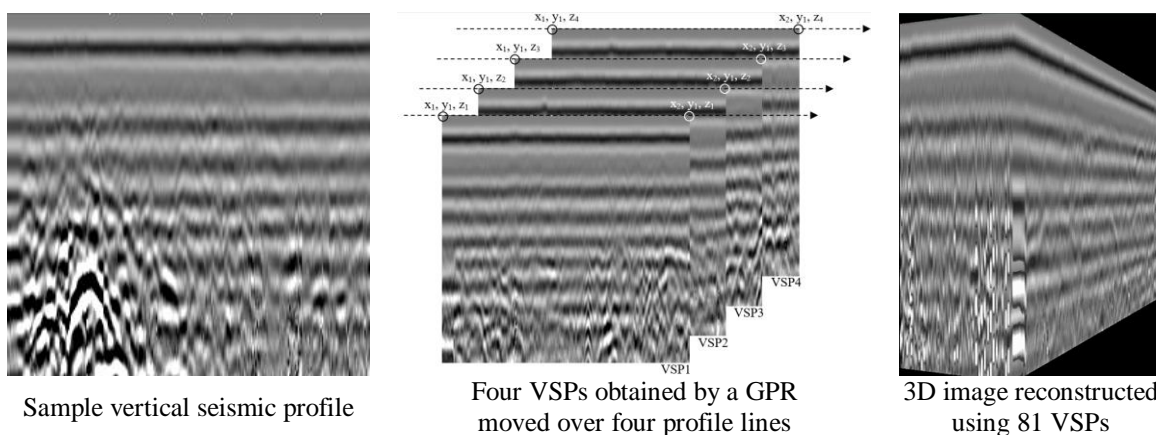


Fig. 4: A 2D radargram of size 256×256 obtained using a GPR and a set of 4 VSPs

Fig. 4 also shows a set of four VSPs obtained by moving a GPR antenna along four parallel profiles and the 3D image by reconstructing it from 81 VSPs obtained by moving a GPR antenna along 81 parallel profiles. The 3D radargram image shown in Fig. 4 is obtained using 'ray casting' technique, which constructs 3D solid image using 81 slices (VSPs) obtained using a GPR and displays the solid image on a 2D monitor. Notion of ray casting is outlined below on need to know basis.

Ray casting technique – Basic principles

Volume ray casting is an image-ordering and volume rendering method. This computes a 2-D

image from the given 3-D image. A ray is cast for each voxel in a 3D image. The color code as well as opacities observed in the path of a ray are accumulated till the ray exits the volume. The accumulated color value is displayed as the 2-D image pixel for every voxel in the 3-D image. Fig 6.9 demonstrates this process pictorially. A 3-D image voxel has a value. The purpose of ray casting is to project a voxel V in a 3D volume image on to a point V' in 2D plane. All the points that lie in this ray overlap at position V' . The opacity α_i and the color value c_i of each point are accumulated and the final color or brightness of a point V' is projected on

to the 2D image plane P. This is illustrated in Fig 5.

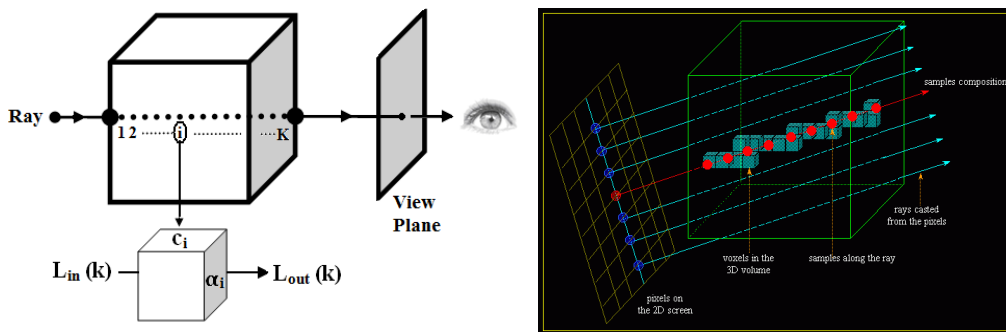


Fig. 5: The process of ray casting

Ray casting allows one to visualize a 3D image on a 2D monitor. The 3D radargram image shown in Fig. 6.8 is also visualized using ray casting method.

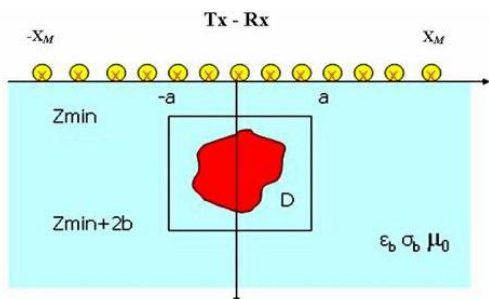
3. Linear Imaging Algorithms for Buried Object Detection

Just as Magnetic Resonance Imaging (MRI) is used for visualizing internal body parts, subsurface imaging is employed for detecting and localizing elements like oil, underground water, minerals, diamonds, precious stones and gems, rare earth elements and buried archeological structures. But in most cases, detection and localization of buried objects is of major concern. This is achieved by using imaging algorithms based on scattering models which are defined by linear equations. It has been found that subsurface imaging algorithms work well in the framework of linear models upon which they are founded. In this thesis, imaging algorithms based on linear models are suggested to be employed in practical scenarios. Such algorithms fall under two categories: (i) *migration algorithms* and (ii) *inverse filtering algorithms*. Subsurface imaging algorithms are essentially signal processing procedures, but most of them address primarily the problem of clutter reduction. The echo signals of a GPR are not only reflections obtained from targeted buried objects but also from

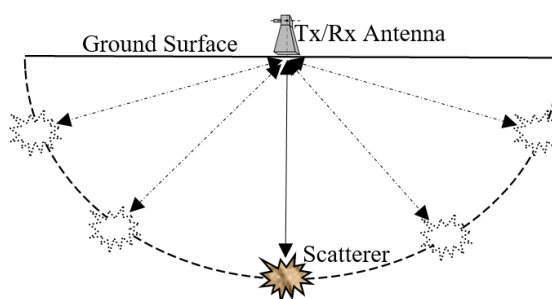
surrounding soil, stones and other unknown elements. Reflected signals from a targeted buried object are used for object detection and localization whereas reflected clutter signals from unwanted surrounding scenario are to be filtered out. Maximum clutter arises from the air-soil interface and one has to use appropriate clutter noise filtering algorithms in order to obtain reasonably good radargram images.

3.1 Migration algorithms

Migration procedures essentially aim at reconstructing buried scattering objects surrounded by air or soil, using measurements made. A mathematical treatise could be developed based on wave equation. Let us assume that the antennas for transmitting and receiving are located at the surface of the ground in a monostatic configuration. In this context, the effects due to air-soil interface is ignored. This means that a homogeneous background scenario is considered with the electromagnetic features of the subsurface. Let us consider a point-like scatterer located in the object space at $\underline{r}_{sc} = (x_{sc}, z_{sc})$ and let us denote the observation variable for the positions where the scattered field is recorded as $\underline{r}_O = (x_O, z_O)$.



Geometry of the subsurface prospecting problem



Hypothetical model of A-scan trace

Fig. 6: Geometry of the subsurface prospecting problem and A-scan trace

With reference to Fig. 6, it is assumed $z_0 = 0$, $x_0 \in [-X_M, X_M]$, where $\Sigma = [-X_M, X_M]$ is the synthesized measurement aperture. $s_T(t)$ is the transmitted impulse signal. Then the corresponding backscattered field is given by

$$s_R(\underline{r}_O, t) = s_T(t - 2\frac{|\underline{r}_O - \underline{r}_{sc}|}{v})$$

where v is the soil propagation speed, which is assumed to be a constant. Here, the amplitude variations due to propagation spreading are ignored. Now, the backscattered signal in the x_0 - t data space will appear as a diffraction hyperbola whose apex is in $(x, 2z/v)$ which can be translated in the x - z image space by exploiting that $x = x_0$ and $z = vt/2$. The hyperbolic output of B-scan is due to the fixed directivity of the antennas. The operation of migration is for compensating the spreading by refocalizing every segment of hyperbola to its apex. In order to do this, the travel-time “ t ” should not be translated directly into depth measure, because equal travel-times formally imply equal distances, whereas the direction of arrival is not used in the calculation. Now for each trace of a position (i.e., A-scan), the scatterer object position should lie theoretically on a semicircle centred on the source-receiver position and whose radius is equal to the distance obtained by multiplying the travel-time by half the wave-speed in the soil. Based on this hypothesis, each x_0 - t data point is equally distributed over a semicircle in the image space, such that all the semicircles intersect at \underline{r}_{sc} . This method is called as *Wave Interference Migration*, which is also known as *A-scan-driven approach*. This technique is useful only when Signal to Noise Ratio (SNR) is guaranteed and that the surrounding scattering scenario is not complex. However, an ensemble of point scatterers is considered and thus linearity of the scattering model seems to be an implicit model.

Alternative method

‘*Diffraction Summation*’ is yet another technique, which is a pixel-driven approach. In this case, the object space is treated as an array of pixels and a diffraction hyperbola is constructed for each pixel in the image data space. Subsequently, each pixel reconstruction is obtained as a sum of all A-scan traces. This will yield a synthesized hyperbola in the image. This is carried out by evaluating the summation integral for each pixel defined by (x, z) .

$$R(x, z) = \int_{\Sigma} \int_T s_R(x_0, t) \delta(t - \frac{2}{v} \sqrt{(x - x_0)^2 + z^2}) dx_0 dt$$

Σ is the measurement aperture and T is the time interval and $R(x, z)$ is the corresponding migrated data. $S_R(x_0, \omega)$ is the Fourier transform of $s_R(x_0, t)$ and

$\exp(-j\omega t)$ is the temporal Fourier kernel. Now $R(x, z)$ is rewritten as

$$R(x, z) = \int_{\Sigma} \int_{\Omega} S_R(x_0, \omega) \exp(j\frac{2\omega}{v} \sqrt{(x - x_0)^2 + z^2}) dx_0 d\omega$$

where Ω is the frequency bandwidth. Now, if $k = \frac{\omega}{v}$, then the equation for $R(x, z)$ becomes

$$R(x, z) = \int_{\Sigma} \int_{\Omega_k} S_R(x_0, k) \exp(j2k \sqrt{(x - x_0)^2 + z^2}) dx_0 dk$$

where Ω_k denotes the frequency band in the k domain. In this case, unwanted scalar factor is ignored. The above equation establishes equivalence between *Diffraction Summation* and the *Range Migration Technique*. In both the cases, convolution in x_0 and an integration in k are used. The convolution is computed using two-dimensional Fourier transform domain as

$$R(x, z) = \int_{\Omega_x} \int_{\Omega_k} f(k_x, k) S_R(k_x, k) \exp(-jk_x x) \exp(jk_z z) dk_x dk$$

where Ω_{kx} is the selected frequency band in the spectrum k_x , $f(k_x, k) = \exp(j\pi/4) k \sqrt{2/(k_x^2 \pi)}$ is the amplitude (where \sqrt{z} is neglected), $k_z = \sqrt{4k^2 - k_x^2}$. $S_R(k_x, k)$ is the Fourier transform with respect to x_0 of $S_R(x_0, k)$ and $\exp(jk_x x)$ is the spatial Fourier kernel, where the Fourier transform of the exponential term is $\exp(j2k \sqrt{x^2 + z^2})$. If one substitutes the frequency wavenumber k by the integration in k_z , then the Fourier transform is rewritten as

$$R(x, z) = \int_{\Omega_x} \int_{\Omega_k} f(k_x, k) \frac{k_z}{\sqrt{k_x^2 + k_z^2}} S_R(k_x, k_z) \exp(-jk_x x) \exp(jk_z z) dk_x dk_z$$

The above equation exhibits considerable computational advantage since it is evaluated using appropriate Fast Fourier Transform (FFT) algorithm for every point in the object space. This also requires data to be interpolated and re-sampled in a rectangular grid in the k_x - k_z spatial spectral domain.

Exploding source model

This is another migration method that involves wave equation. In this case, the scattered field is viewed as primary radiation from excitation source (assumed) rather than as secondary reradiation from passive source (actual). Now, the scattered field outside the source is a solution of the frequency domain based wave equation $\nabla^2 S_R(x, \omega) + 4k^2 S_R(x, \omega) = 0$ where $\nabla \equiv (\frac{\partial}{\partial x}, \frac{\partial}{\partial z})$, and $S_R(x, \omega)$ is the Fourier transform of $s_R(x, t)$. Now, one obtains the field spatial spectrum as $S_R(k_x, \omega, z) = S_R(k_x, \omega, z') \exp[jk_z(z - z')]$, where k_z is the same wave number as defined previously; but with the exception that only the up-travelling waves, that is, the wave travelling along the

negative z direction is considered. Accordingly, the field in the object space is determined by assuming boundary condition over the measurement line at $z = 0$. Finally, the superimposition along frequency ω is obtained as

$$R(x, z) = \int_{\Omega_x} \int_{\Omega} S_R(k_x, \omega) \exp(-jk_x x) \exp(jk_z z) dk_x d\omega$$

This is called *F-K Migration*, which is a generalization of the *Doppler compression technique* used in SAR imaging. This technique is also referred to as *Phase Shift Migration*. *Phase Shift Migration* is similar to *Summation Diffraction* technique and it is expressed as a Fourier double integral in the spatial/spectral domain. Unlike the migration technique described earlier where field is back-propagated, *Phase Shift Migration* assumes field as radiated by a localized source. Hence, the field “extrapolation” in the object space works as long as the scatterers are reached. It is obvious for the scatterers, which are buried within a dispersive and dissipative medium. The inverse Fourier transform with respect to k_x is

$$R(x, z) = \int_{\Sigma} \int_{\Omega} s_R(x_O, z = 0, \omega) \frac{\partial}{\partial z} G^*(x - x_O, z, \omega) dx_O d\omega$$

where G^* is the complex conjugated Green’s function. This migration scheme is known as *Rayleigh-Sommerfeld holography*, which is a specific case of *Generalized Holography* founded on the basis of Porter-Bojarski integral equation. The time domain version of the above equation is called as *Kirchhoff Migration*. Now, $R(x, z)$ is further expressed as

$$R(x, z) \cong \int_{\Sigma} \int_{\Gamma} \cos(-\hat{z}, \underline{r}_{Oc}) s_R(x_O, t) \frac{\partial}{\partial t} \delta(t - \frac{2}{v} \sqrt{(x - x_O)^2 + z^2}) dx_O$$

where $\cos(-\hat{z}, \underline{r}_{Oc})$ is the angle between the unit normal vector at the measurement line and the vector $\underline{r}_{Oc} = \sqrt{(x - x_O)^2 + z^2}$.

Scattering equations and the Born approximation

So far, various migration algorithms have been proposed and used as models that make use of Fourier transform operators. In any case, the migrated field and the scatterers to be reconstructed have not been formally linked and hence this problem remained just supported by intuitive arguments. To find a solution to this problem, one needs to deal with those equations, which describe the scattering phenomenon accurately. Therefore, the subsurface imaging problem is to be viewed as an inverse scattering problem, where one tries to infer the electromagnetic properties of the scatterer from the scattered field measured outside the scatterer. Now, the problem is restated as “Given an incident field, E_{inc} , that is the electromagnetic field

in the background medium without the scattering object and generated by a known source, the scattered field E_s is established as a result of interaction with the object. Now, from the knowledge of E_s , some geometrical or structural properties about the scatterer, have to be obtained”.

In order to do this, a procedure is shown here with the help of a case study. A cylindrical dielectric object enclosed within the domain D is illuminated by a linearly polarized incident field along the axis and the scattered field observed in the domain Σ . The equivalent dielectric permittivity function of the unknown object and that of the background medium are denoted by $\varepsilon(r)$ and $\varepsilon_b(r)$ respectively. In fact, $\varepsilon_b(r)$ need must be constant because of the non-homogeneous background medium. The magnetic permeability of the free space μ_0 is assumed everywhere. Thus, the problem boils down to retrieving the dielectric permittivity profile $\varepsilon(r)$ of the unknown object using the knowledge of E_s . The frequency domain relationship between the data and the unknown is furnished by the Helmholtz equation $\nabla^2 E + k_b^2 E = -k_b^2 \chi(r) E$ where $E = E_{inc} + E_s$ is the total field, k_b is the subsurface wave-number and $\chi(r) = \varepsilon(r)/\varepsilon_b - 1$ is the dimensionless contrast function. Now, one obtains pair of scalar integral equations using Green’s function method as

$$E(\underline{r}, \underline{r}_S; k_b) = E_{inc}(\underline{r}, \underline{r}_S; k_b) + k_b^2 \int_D G(\underline{r}, \underline{r}'; k_b) E(\underline{r}', \underline{r}_S; k_b) \chi(\underline{r}') d\underline{r}' \quad \underline{r} \in D$$

$$E_s(\underline{r}_O, \underline{r}_S; k_b) = k_b^2 \int_D G(\underline{r}_O, \underline{r}; k_b) E(\underline{r}, \underline{r}_S; k_b) \chi(\underline{r}) d\underline{r} \quad \underline{r}_O \in \Sigma$$

where G is Green’s function, \underline{r}_O is the observation point and \underline{r}_S is the position of the source. Now, the above integral equations allow one to interpret the scattered field as radiated by secondary sources, which are located within the spatial region of scatterers. Contrast function is obtained by inverting the pair of equations, and this is known as the reconstruction problem. The field inside the scatterers defined by the first equation depends on the unknown contrast function, and thus the relationship between contrast function and scattered field is said to be nonlinear. However, one can assume $E \cong E_{inc}$ within the scatterer region and obtain the Born linear model. Consequently, the scattering model becomes a linear approximation

$$E_s(\underline{r}_O, \underline{r}_S; k_b) = k_b^2 \int_D G(\underline{r}_O, \underline{r}; k_b) E_{inc}(\underline{r}, \underline{r}_S; k_b) \chi(\underline{r}) d\underline{r} \quad \underline{r}_O \in \Sigma$$

In such a case, the internal field need not depend on the dielectric profile. This amounts to saying that one can ignore mutual interactions between different parts of the object and also between different objects. In other words, each part of the scatter object is treated as an elementary scatterer independent of the other scatterers. If one considers a homogeneous background medium and a monostatic type of data collection, where $\underline{r}_O = \underline{r}_S$

, the linearized scatter model equation could be rewritten as

$$E_S(r_O; k_b) = k_b \int_D \frac{\exp(-2jk_b|r_O - r|)}{|r_O - r|} \chi(r) dr \quad r_O \in \Sigma$$

In such a case, a two-dimensional filamentary current $I(\omega) \propto 1/\omega$ is assumed as source of the incident field. For the measurement aperture Σ the scatter field equation turns out to be

$$E_S(x_O; k_b) = k_b \int_D \frac{\exp[-2jk_b\sqrt{(x_O - x)^2 + z^2}]}{\sqrt{(x_O - x)^2 + z^2}} \chi(x, z) dx dz$$

The Fourier transform of the scattered field with respect to x_O is obtained using the plane-wave spectrum of the Green's function as

$$E_S(k_x, k_b) = \frac{k_b}{k_z} \hat{\chi}(k_x, k_z) \text{ with } k_z = \sqrt{4k_b^2 - k_x^2}. \text{ When the}$$

spatial Fourier transform data are arranged in the k_x-k_z spectral plane, then the contrast function is obtained as

$$\tilde{\chi}(x, z) = \int_{\Omega_{k_x}} \int_{\Omega_{k_z}} \frac{k_z}{\sqrt{k_x^2 + k_z^2}} E_S(k_x, k_z) \exp(-jk_x x) \exp(jk_z z) dk_x dk_z$$

It is important to note that this equation coincides with that of *F-K Migration* when ω is replaced by k_z . Therefore, using linear Born approximation a connection between the migrated field and scatterers is established in terms of contrast functions. Similar results may also be obtained for various kinds of scatterers where linear approximations are adopted.

3.2 Inverse filtering imaging algorithms

As discussed earlier, for a two-dimensional and scalar geometry, the scattering phenomenon is modelled using a linear scalar operator $A : \chi \in X \rightarrow E_S \in E$ where χ is the contrast function and E_S is the scattered field. X and E represent the sets pertaining to the contrast function and the scattered field data respectively. In fact, they are Hilbert spaces of square integrable (finite energy) functions, the first one is of complex valued functions defined on D , and the second one of functions supported over $\Lambda = \Sigma \times \Omega$. As far as the Dirichlet's conditions to be satisfied by a signal for applying Fourier transform to it are (i) the signal should be absolutely integrable and square integrable. A signal is considered as a subspace of a Hilbert space $L^{-\infty, +\infty}$ and a signal processing system as a bounded linear operator $\phi : L^{-\infty, +\infty} \rightarrow L^{-\infty, +\infty}$. Hilbert space representations of X and E as square integrable functions allows one to assume that no a priori information is available other than that the finiteness of its energy is due to physical considerations. Moreover, it ensures that E is wide enough to accept effects due to uncertainties and noise in the data. Then, the problem calls for inverting scatter field equation to obtain contrast function. The kernel in the scatter field equation is a

continuous function on $X \times E$, and so the linear operator is compact. This means that the inverse problem is indeed an ill-posed problem. For any compact, non-symmetric operator, singular value decomposition is a sufficiently powerful tool to solve the problem. The singular system of operator A is denoted as $\{\sigma_n, u_n, v_n\}_{n=0}^{\infty}$. In short, $\{\sigma_n\}_{n=0}^{\infty}$ is the sequence of singular values ordered in a non-increasing way, where $\{u_n\}_{n=0}^{\infty}$ and $\{v_n\}_{n=0}^{\infty}$ are orthonormal sets of functions which offer solution to the eigenvalue problems

$$A u_n = \sigma_n v_n$$

$$A^+ v_n = \sigma_n u_n$$

where A^+ is the adjoint operator of A , which spans the orthogonal complement of the kernel of A , that is $N(A)^\perp$, and the closure of the range of A , that is $\overline{R(A)}$, respectively. A formal solution is given by

$$\chi = \sum_{n=0}^{\infty} \frac{\langle E_S, v_n \rangle_E}{\sigma_n} u_n, \text{ where } \langle \cdot, \cdot \rangle_E \text{ denotes the scalar}$$

product in the data space E . Because A is compact, $R(A)$ is not a closed set. This implies that the Picard's conditions are not fulfilled for any data function; thus, the solution may not exist and if at all it exists, it need not depend continuously on data. This is a mathematical validation for the ill-posedness of the problem. In addition, one has to account for another problem of actual data corrupted by various uncertainties and noise n . Hence the contrast function becomes

$$\tilde{\chi} = \sum_{n=0}^{\infty} \frac{\langle E_S, v_n \rangle_E}{\sigma_n} u_n + \sum_{n=0}^{\infty} \frac{\langle n, v_n \rangle_E}{\sigma_n} u_n$$

Now, due to compactness, singular values tend to zero and their index increases. This means that, the second term $\sum_{n=0}^{\infty} \frac{\langle n, v_n \rangle_E}{\sigma_n} u_n$ in the above equation does

not converge and it thus yields an unstable solution. Even a small error in the data is amplified by singular values that are close to zero. This lacuna can be rectified only by regularizing the ill-posed inverse problem. For instance, this is achieved by discarding projections of data on the singular functions corresponding to less significant singular values, and it is done by filtering out singular functions corresponding to singular values below a user specified threshold. This scheme is called as **Truncated Singular Value Decomposition (TSVD)** and it is the modest method meant for a large class of windowing based regularizing schemes. As a result, the finite-dimensional approximate but stable solution is given by $\tilde{\chi} = \sum_{n=0}^{N_r} \frac{\langle E_S + n, v_n \rangle_E}{\sigma_n} u_n$. The

fundamental application of regularization theory is to substitute a given ill-posed problem by a well-posed problem, based on a parameter α , from among a family of well posed problems defined by $\chi = A_\alpha^n E_S$. In the case of *Truncated Singular Value Decomposition* method (TSVD), α corresponds to

the threshold N_T and the noise level n , so that a compromise between accuracy and stability is obtained. When $n \rightarrow 0$ and $\alpha \rightarrow 0$, the regularized reconstruction would tend to a generalized inverse. In practice, **Tikhonov regularization scheme** is used widely, because it has the advantage of using a priori information about the unknown. In this case, the inversion problem is defined as a constrained optimization problem $\tilde{\chi} = \min\{\|A\chi - E_s\|^2 + \alpha\|E_s\|^2\}$. The minimization constraint arises from a priori information and it may be different from the energy constraint outlined earlier. Another scheme called **Landweber regularization** advocates that the first kind integral equation be inverted as a second kind integral equation such that a well-posed problem is obtained. Consequently, the optimization problem is recast as $\tilde{X} = A^+ E_s + (I - A^+ A E_s)\chi$, and a solution obtained using an iterative procedure. The regularization parameter, in this case, is the number of iterations employed in the minimization procedure. All these regularization schemes could be compared in terms of the operator properties. This is done by expressing them in terms of singular system. Then, Tikhonov regularization is expressed as $\tilde{\chi} = \sum_{n=0}^{\infty} \frac{\sigma_n}{\sigma_n^2 + \alpha} (E_s, v_n)_E u_n$ and Landweber method as $\tilde{\chi} = \sum_{n=0}^{\infty} \frac{1 - (1 - \sigma_n^2)^{N_i}}{\sigma_n} (E_s, v_n)_E u_n$. One can see that all these regularization methods ultimately turn out to be the unknown spectral filters. For the sake of computational convenience one can choose a suitable parameter for a regularization algorithm, and the question is how to choose the parameter. As specified earlier, this parameter choice is done based on the noise level, the mathematical features of the

operator to be inverted and the available a priori information about the unknown. Several methods exist for regularization parameter selection. Such methods make use of the knowledge about noise level, like the Morozov discrepancy principle, or some generalized cross validation technique if noise level is not of concern.

Singular system formalism could also be used to compare the migration and inverse filtering techniques. One may observe that the **Diffraction Summation** migrated field reconstruction corresponds substantially to attain inversion by means of adjoint operator, that is $\tilde{\chi} = A^+ E_s$ which is expressed in terms of singular system as $\tilde{\chi} = \sum_{n=0}^{\infty} \sigma_n (E_s, v_n)_E u_n$. One may also observe that migration allows one to have a stable reconstruction because the singular values appear in the numerator. In practice, this involves an *intrinsic* limit on the resolution in the reconstructions regardless of noise levels. Now, χ and its reconstructed version $\tilde{\chi}$ are related by the integral

$$\tilde{\chi}(x, z) = \int_D K(x, z; x' z') \chi(x', z') dx' dz'$$

where $K(x, z; x' z')$ is called *model resolution kernel*. So, the model resolution kernel tends to a Dirac delta, that is, $K(x, z; x' z') \rightarrow \delta(x - x', z - z')$, when noise is absent and $\alpha \rightarrow 0$. Therefore, inverse filtering can provide better resolution in the reconstructions, but that depends on the noise level. Fig. 7 shows reconstruction performances of TSVD and F-K migration for a point-target.

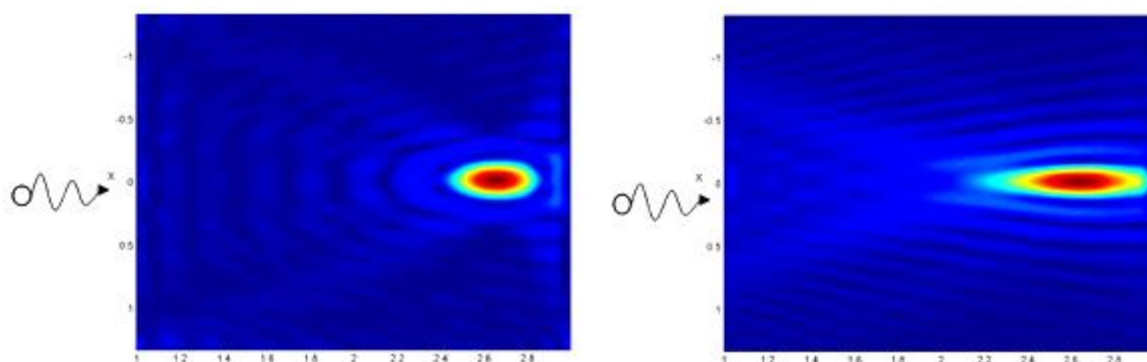


Fig. 7: Comparison between TSVD (left) and F-K migration (right)

So far, the theory of buried point object detection using GPR has been described to certain extent. The question arises here whether one can theorize a multi-object detection by GPR.

Non-Linear Imaging of Buried Multi-Object Detection

Neither F-K Migration algorithms nor TSVD algorithms would be of any use in the case of detecting multiple objects buried under the ground at different depths. In such cases, the receiver antenna of a GPR will receive multiples of echoes

from the scatterers and the onboard computer should integrate all such echoes received at a particular position fixed by GPS coordinates. Ground Penetration Radar (GPR) is used for excitation. Excitation is applied at appropriate locations,

preferably at the centers of the sub divided regions of the area to be prospected. Fig. 8 shows excitation process as a serpentine scanning of a rectangular subsampled field model.

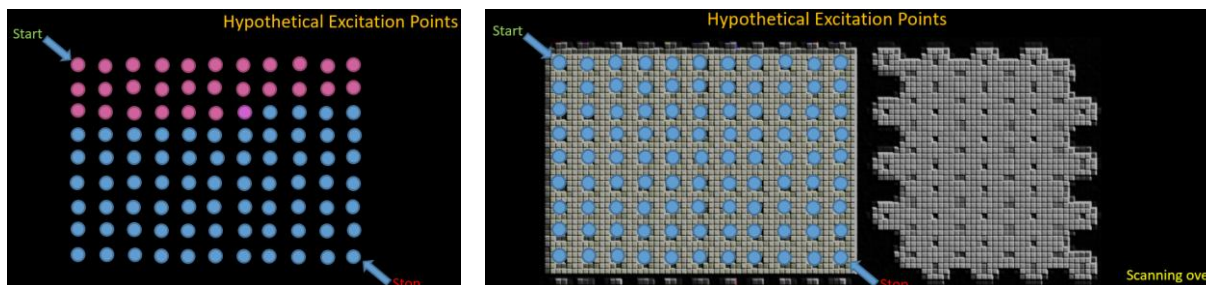


Fig. 8: Excitation process as a serpentine scanning of rectangular field model

Area of a sub divided region determines the resolution. The intensity of excitation depends on many factors but mainly on the required depth of penetration. A short duration pulse is applied as excitation and the echo received and registered for

further analysis. With reference to Fig. 8, one would obtain 99 echoes in the form of one-dimensional characteristic signals. Fig. 9 presents a hypothetical diagram showing more than one buried object.

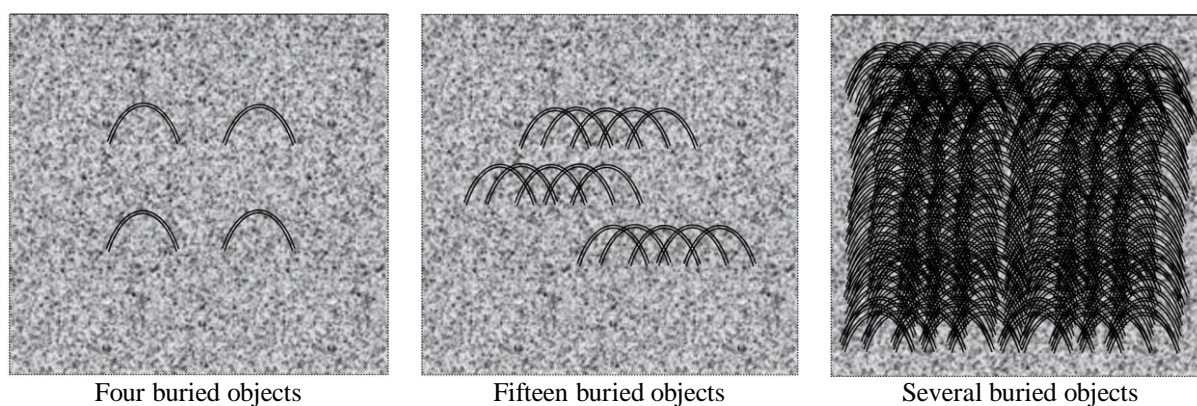
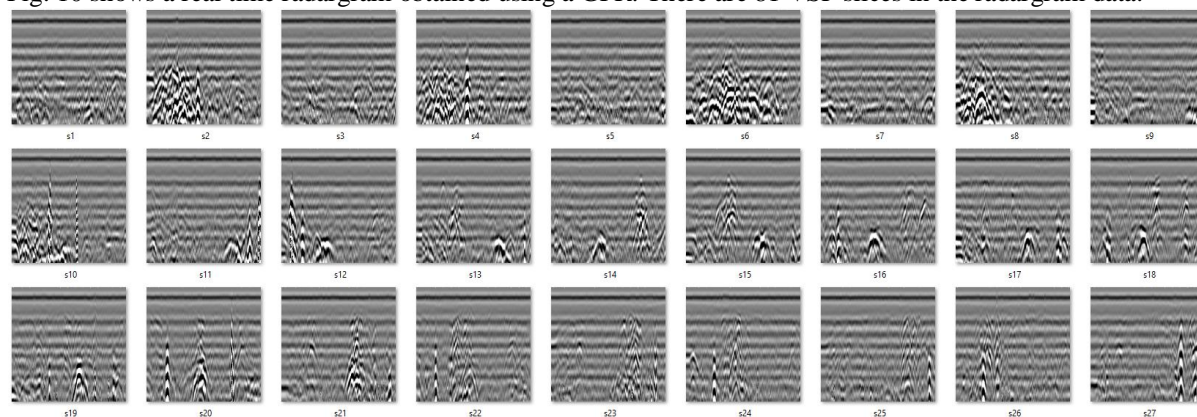


Fig. 9: Multiple objects buried under ground and at different depths

Fig. 10 shows a real time radargram obtained using a GPR. There are 81 VSP slices in the radargram data.



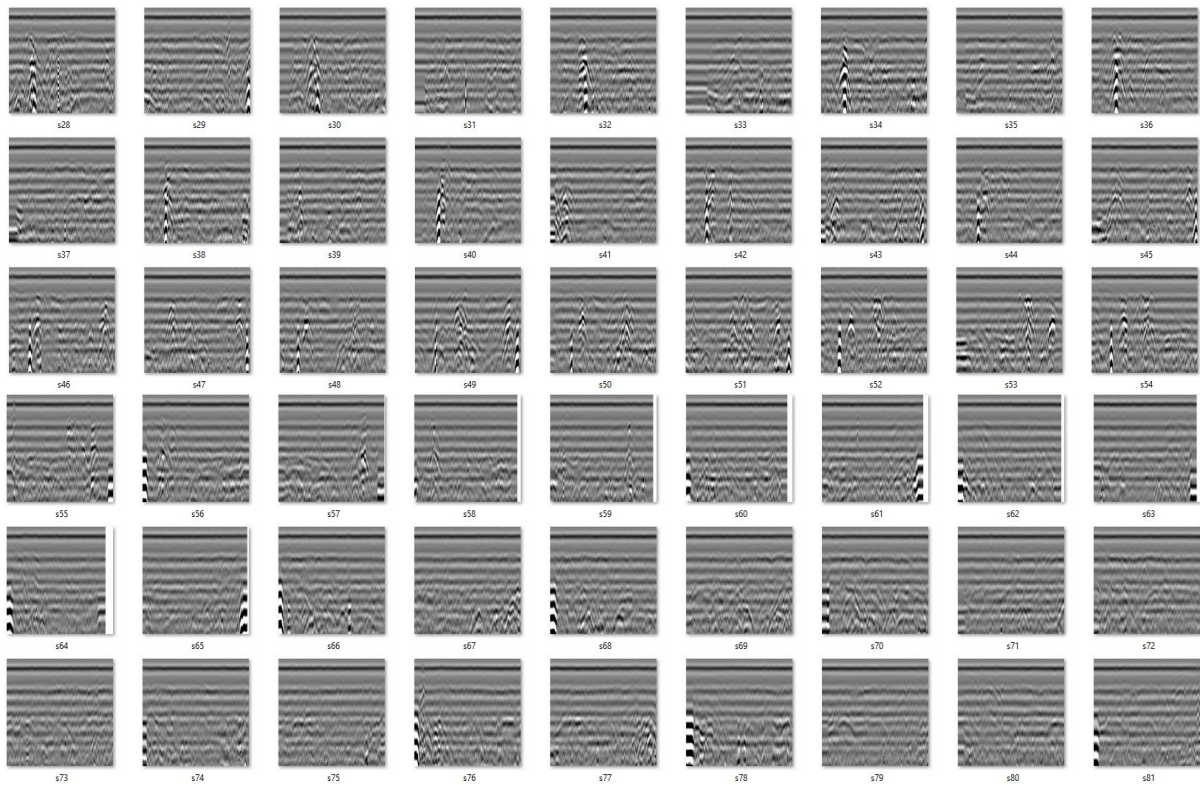
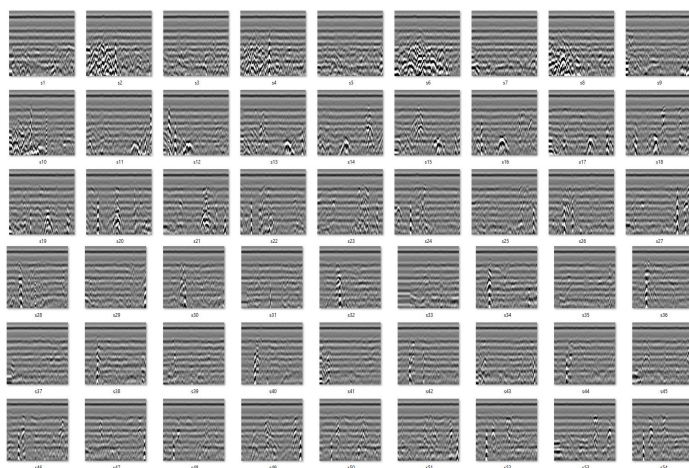


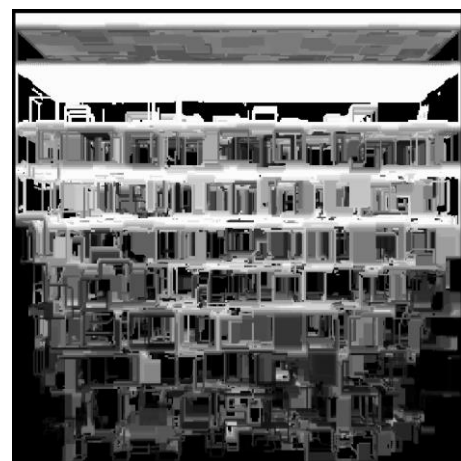
Fig. 10: Realtime radargram containing 81 slices obtained by a GPR

Using ray casting method, one can reconstruct a 3D model image from all these 81 slices. The 3D radargram obtained from using a GPR does not show any meaningful visualization. One has to explore the possibilities of interpreting 3D radargrams using suitable 3D image processing

and pattern recognition techniques. Fig. 11 shows the first 54 VSP slices and the processed version of the 3D radargram. Fig. 12 shows the 3D model obtained by ray casting method and the processed version of the 3D radargram with left and right oblique views.

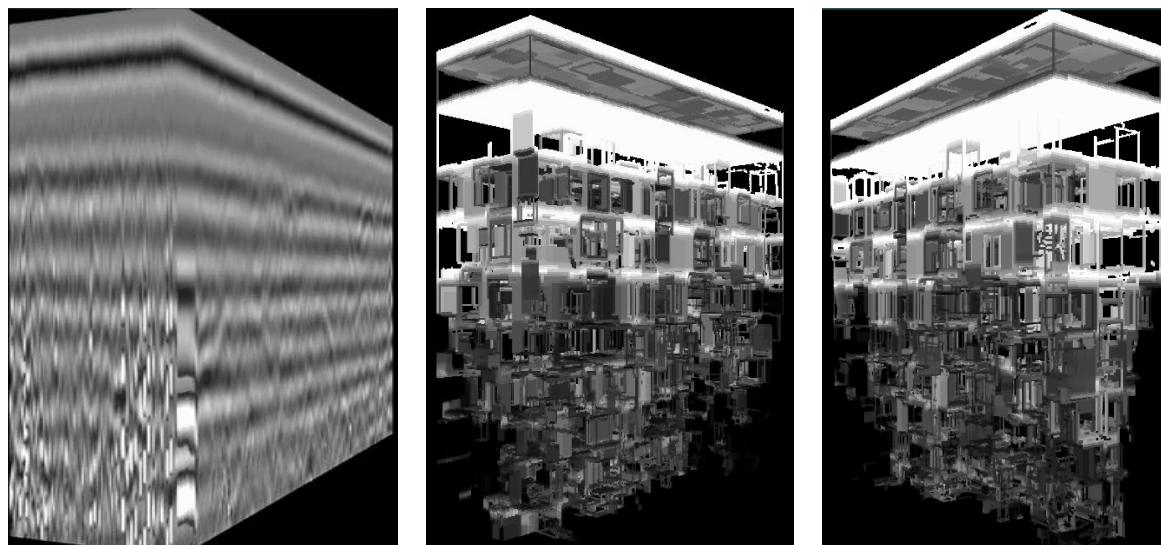


80 VSP slices obtained using a GPR



Processed 3D image

Fig. 11: The first 54 VSP slices and the processed version of the 3D radargram



3D radargram from 81 slices

Left anterior oblique view

Right anterior oblique view

Fig. 12: 3D radargram and its processed versions with left and right oblique views

Details of processing 3D radargrams are not in the scope of this paper and hence not provided.

Advisory Committee Members and Co-authors

1. Dr. Manish Prateek, Dean, School of Computer Science, UPES, Dehradun, India
2. Dr. Amit Agarwal, Director, APJ Abdul Kalam, Institute of Technology, Dehradun, India
3. Dr. Michael Patrick Coyle, Chief Executive Officer, Avatar MedVision US LLC, NC, USA
4. Sathya Govindarajan, Director, Pentagram Research Centre Private Limited, Hyderabad, India
5. Prashanthi Govindarajan, Director, Pentagram Research Centre Private Limited, Hyderabad, India
6. Yashaswi Vemuganti, Consultant, Avatar MedVision US LLC, NC, USA
7. Dr. Jean Claude Perez, IBM European Research Center on Artificial Intelligence, France
8. Dr. Hindupur Rajasimha, Chief Engineer, Indian Space Research Organization and IDBI (Retd.)

REFERENCES

- [1]. Jean Serra; Cube, cube-octahedron or rhomb-dodecahedron as bases for 3-D shape descriptions, *Advances in visual form analysis*, World Scientific 1997, 502-519.
- [2]. Wuthrich, C.A. and Stucki, P.; An algorithm comparison between square- and hexagonal based grids; *Graphical Models and Image Processing*, 53(4), 324-339, 1991.
- [3]. Reinhard Klette and Azriel Rosenfeld; *Digital Geometry: Geometric methods for picture analysis*; Elsevier, 2004.
- [4]. B. Nagy; Geometry of Neighborhood sequences in hexagonal grid; *Discrete Geometry of computer imagery*; LNCS-4245, Springer.
- [5]. Tristan Roussillon, Laure Tougne, and Isabelle Sivignon; What Does Digital Straightness tell about Digital Convexity?;
- [6]. Edward Angel, "Interactive Computer Graphics- a top down approach with OpenGL", Second Edition, Addison Wesley, 2000.
- [7]. S.W. Zucker, R.A. Hummel, "A Three-Dimensional Edge Operator", *IEEE Trans. On PAMI*, Vol. 3, May 1981.
- [8]. Jürgen, H., Manner, R., Knittel, G., and Strasser, W. (1995). Three Architectures for Volume Rendering. *International Journal of the Eurographics Association*, 14, 111-122
- [9]. Dachille, F. (1997). *Volume Visualization Algorithms and Architectures*. Research Proficiency Examination, SUNY at Stony Brook
- [10]. Günther, T., Poliwoda, C., Reinhart, C., Hesser, J., and Manner, J. (1994). VIRIM: A Massively Parallel Processor for Real-Time Volume Visualization in Medicine. *Proceedings of the 9th Eurographics Hardware Workshop*, 103-108
- [11]. Boer, M.De, Gröpl, A., Hesser, J., and Manner, R. (1996). Latency-and Hazard-free Volume Memory Architecture for Direct Volume Rendering. *Eurographics Workshop on Graphics Hardware*, 109-119
- [12]. Swan, J.E. (1997). *Object Order Rendering of Discrete Objects*. PhD. Thesis, Department of Computer and Information Science, The Ohio State University

- [13]. Yagel, R. (1996). Classification and Survey of Algorithms for Volume Viewing. SIGGRAPH tutorial notes (course 34)
- [14]. Law, A. (1996). Exploiting Coherency in Parallel Algorithms for Volume Rendering. PhD. Thesis, Department of Computer and Information Science, The Ohio State University
- [15]. Ray, H., Pfister, H., Silver, D., and Cook, T.A. (1999). Ray Casting Architectures for Volume Visualization. IEEE Transactions on Visualization and Computer Graphics, 5(3), 210-233
- [16]. Yagel, R. (1996). Towards Real Time Volume Rendering. Proceedings of GRAPHICON' 96, 230-241
- [17]. Kaufman, A.E. (1994). Voxels as a Computational Representation of Geometry. in The Computational Representation of Geometry SIGGRAPH '94 Course Notes
- [18]. Lacroute, P., and Levoy, M. (1994). Fast Volume Rendering Using a Shear-Warp Factorization of the Viewing Transform. Computer Graphics Proceedings Annual Conference Series ACM SIGGRAPH, 451-458.
- [19]. Sutherland, I.E., Sproull, R.F., and Schumaker, R.A. (1974) A Characterization of Ten Hidden Surface Algorithms. ACM Computing Surveys, 6(1), 1-55
- [20]. Roberts, J.C. (1993). An Overview of Rendering from Volume Data including Surface and Volume Rendering. Technical Report 13-93*, University of Kent, Computing Laboratory, Canterbury, UK.
- [21]. Frieder, G., Gordon, D., and Reynolds, R.A. (1985). Back-to-Front Display of Voxel-Based Objects. IEEE Computer Graphics and Applications, 5(1), 52-60
- [22]. Westover, A.L. (1991). Splatting: A Parallel Feed-Forward Volume Rendering Algorithm. Ph.D. Dissertation, Department of Computer Science, The University of North Carolina at Chapel Hill
- [23]. Zwicker, M., Pfister, H., Baar, J.B. and Gross M. (2001). Surface Splatting. In Computer Graphics SIGGRAPH 2001 Proceedings, 371-378
- [24]. Nulkar, M., and Mueller, K. (2001). Splatting With Shadows. International Workshop on Volume Graphics 2001, 35-50
- [25]. J. Krüger and R. Westermann, Acceleration Techniques for GPU-based Volume Rendering, Proceedings of the 14th IEEE Visualization 2003 (VIS'03), 38-43.
- [26]. Markus Hadwiger, Joe M. Kniss, Christ of Rezk-salama, Daniel Weiskopf, and Klaus Engel. Real time Volume Graphics. A. K. Peters, Ltd., USA, 2006.
- [27]. Goodman, D., Nishimura, Y., Hongo, H and Noriaki N., 2006. Correcting for topography and the tilt of the GPR antenna, Archaeological Prospection, 13: 157-161.
- [28]. Goodman, D., Y. Nishimura, and J. D. Rogers, 1995. GPR time slices in archaeological prospection: *Archaeological Prospection*, 2:85-89.
- [29]. Goodman, D., 1994. Ground-penetrating radar simulation in engineering and archaeology: *GEOPHYSICS*, 59:224-232.